Influence of Rotational Distortions on Li^+- and Na^+-Intercalation in Anti-NASICON $Fe_2(MoO_4)_3$

Journal:	*Chemistry of Materials*
Manuscript ID	cm-2016-01806p.R1
Manuscript Type:	Article
Date Submitted by the Author:	n/a
Complete List of Authors:	Zhou, Shiliang; University of Southern California, Chemistry Barim, Gözde; University of Southern California, Department of Chemistry Morgan, Benjamin; University of Bath, Chemistry Melot, Brent; University of Southern California, Chemistry Brutchey, Richard; University of Southern California, Department of Chemistry

Influence of Rotational Distortions on Li^+- and Na^+-Intercalation in Anti-NASICON $Fe_2(MoO_4)_3$

Shiliang Zhou,[†,§] Gözde Barim,[†,§] Benjamin J. Morgan,[‡] Brent C. Melot,[†,*] and Richard L. Brutchey[†,*]

[†]*Department of Chemistry, University of Southern California, Los Angeles, CA 90089, USA*

[‡]*Department of Chemistry, University of Bath, Claverton Down, UK*

E-mail: melot@usc.edu, brutchey@usc.edu

Abstract

Anti-NASICON $Fe_2(MoO_4)_3$ ($P2_1/c$) shows significant structural and electrochemical differences in the intercalation of Li^+ and Na^+ ions. To understand the origin of this behavior, we have used a combination of *in-situ* X-ray and high-resolution neutron diffraction, total scattering, electrochemical measurements, density functional theory calculations, and symmetry-mode analysis. We find that for Li^+-intercalation, which proceeds via a two-phase monoclinic-to-orthorhombic (*Pbcn*) phase transition, the host lattice undergoes a concerted rotation of rigid polyhedral subunits driven by strong interactions with the Li^+ ions, leading to an ordered lithium arrangement. Na^+-intercalation, which proceeds via a two-stage solid solution insertion into the monoclinic structure, similarly produces rotations of the lattice polyhedral subunits. However, using a combination of total neutron scattering data and density-functional theory calculations, we find that while these rotational distortions upon Na^+ intercalation are fundamentally the same as for Li^+ intercalation, they result in a far less coherent final structure, with this difference attributed to the substantial difference between the ionic radii of the two alkali metals.

Introduction

The demand for rechargeable lithium- or sodium-ion batteries will continue to grow as renewable energy sources are integrated into the electrical grid, and electric vehicles continue to be developed.[1–3] In rechargeable ion batteries, positive electrode materials undergo reversible intercalation, displacement, or conversion processes to store electricity.[4,5] Present state-of-the-art positive intercalation electrodes for Li^+ or Na^+ ion batteries rely on either layered oxides, spinel oxides, or polyanionic compounds.[6] Polyanionic compounds have structural frameworks composed of corner-sharing polyhedral subunits. This allows much greater lattice flexibility than in layered or spinel oxides, and contributes to noteworthy structural stability with respect to electrochemical cycling. Polyanionic compounds are also considered to be safer than alternative oxides, because they do not release oxygen upon decomposition, which can exacerbate thermal runaway during cell failure.[7,8] Because the utility of polyanionic cathodes is linked to the intrinsic flexibility of their host lattice, the development of next-generation polyanionic electrodes requires understanding the relevant structural distortions that occur across multiple polyanionic compounds as Li^+ and Na^+ are inserted.

NASICON-related structures, with general formula $MM'(XO_4)_3$, were among the first polyanionic compounds investigated as intercalation electrodes.[7] The structures feature large interstitial voids formed by three-dimensionally connected polyhedra, creating a robust structural topology. The chemical versatility of these materials structures means substitution of the polyanionic group can be exploited to tune the position of the redox couples.[9,10] Anti-NASICON $Fe_2(MoO_4)_3$ is a promising cathode for both Li^+ and Na^+ ion cathodes, owing to its highly reversible accommodation of intercalated ions.[11–14] $Fe_2(MoO_4)_3$ crystallizes in a

thermodynamically preferred, low-temperature monoclinic ($P2_1/c$) structure that consists of FeO_6 octahedra and MoO_4 tetrahedra interconnected through corner sharing oxygen atoms (Figure 1). The basic motif of the structure is described as the "lantern unit", composed of three MoO_4 tetrahedra that connect two FeO_6 octahedra (Figure 1b). In the anti-NASICON structure, these units stack in an antiparallel fashion along the ($2b$ + c). In contrast, in the NASICON structure equivalent units stack in a parallel fashion along the c-axis.[7]

While the electrochemical performance of Li^+ and Na^+ (de)insertion into $Fe_2(MoO_4)_3$ has been studied previously, the existing knowledge in the literature is often contradictory, and the mechanism of structural transformations from the parent phase to the intercalated phase remains unknown for monoclinic $Fe_2(MoO_4)_3$. Nadiri *et al*. reported a single-phase structural change in monoclinic $Fe_2(MoO_4)_3$ during Na^+ (de)insertion in the composition ranges of $0.3 \leq x \leq 1.0$ and $1.10 \leq x \leq 1.60$ for $Na_xFe_2(MoO_4)_3$.[12] In contrast, Bruce *et al*. reported the presence of two phases throughout the composition range of $0 < x < 2$ through *ex-situ* X-ray diffraction of powder samples that were electrochemically intercalated.[13] Recent studies by Yue *et al*. reported a two-phase structural change for Li^+ (de)insertion, but a single-phase process for Na^+-intercalation in the high-temperature, orthorhombic (not monoclinic) polymorph of $Fe_2(MoO_4)_3$.[15] To reconcile these various conflicting reports, it is crucial to understand the mechanism by which the structural framework transforms in order to accommodate the intercalation of guest ions.

Herein, we present an investigation into the different insertion behaviors of Li^+ and Na^+ in monoclinic $Fe_2(MoO_4)_3$, with an emphasis on the reorganization of the rigid polyhedral units within the structure framework upon insertion. We have used a combination of structural and electrochemical tools, coupled with an analysis of symmetry-

allowed distortions, to characterize the relationship between the structural evolution of $Fe_2(MoO_4)_3$ during (de)insertion of Na^+ and Li^+ and their corresponding electrochemical properties. We find the insertion processes for Li^+ and Na^+ differ in the ability of rigid MoO_4 tetrahedra to rotate in order to accommodate the presence of guest ions within the lattice framework. This mechanism, whereby intercalation proceeds through cooperative rotations, is found to be strongly influenced by the size and nature of the alkali ion. This result, therefore, may be also relevant to other polyanionic electrodes and, more broadly, to intercalation into any system containing a mixture of rigid and soft bonding units.

Experimental

Synthesis of $Fe_2(MoO_4)_3$

$Fe_2(MoO_4)_3$ was synthesized by a solid-state precipitation method.[16] $(NH_4)_6Mo_7O_{24}{\cdot}4H_2O$ (1.0 mmol) and $Fe(NO_3)_3{\cdot}9H_2O$ (4.65 mmol) were dissolved separately in 100 mL and 50 mL of H_2O, respectively. 0.4 mL of $NH_3{\cdot}H_2O$ was added to the molybdate solution to establish basic conditions. The $Fe(NO_3)_3$ solution was then slowly added to the molybdate solution with stirring, resulting in a yellow precipitate. The reaction mixture was stirred overnight. The resulting yellow precipitate was collected and washed with ethanol by sonicating for 30 min, and isolated by centrifugation (6000 rpm for 15 min). This washing procedure was repeated twice. The resulting $Fe_2(MoO_4)_3$ powder was dried in a vacuum oven at 60 °C for 5 h. The dried $Fe_2(MoO_4)_3$ was then ground with a mortar and pestle and annealed at 400 °C for 6 h in air. A yellowish-green powder was obtained.

Chemical insertion

$Li_2Fe_2(MoO_4)_3$ was prepared by stirring 1.0 g $Fe_2(MoO_4)_3$ in fivefold stoichiometric excess of LiI (dissolved in dry acetonitrile) for 2 weeks. For Na^+ insertion, a sodium

napthalenide solution was prepared by dissolving 3.0 g of Na metal and 1.5 g of naphthalene in 75 mL of dry THF. $Na_2Fe_2(MoO_4)_3$ was prepared by mixing 1.0 g $Fe_2(MoO_4)_3$ in 25 mL of the resulting sodium napthalenide solution for a week.

Structural characterization

Laboratory powder X-ray diffraction (XRD) data was collected on a Bruker D8 diffractometer with a $Co_{K\alpha}$ source (λ_1 = 1.78897 Å, λ_2 = 1.79285 Å), equipped with a LynxEye detector. The collection process was kept the same for different samples using a 0.6 mm slit with a step size 0.02 degrees and a total collection time of 1 h in the 2θ range from 10 to 60 degrees. A Swagelok-type electrochemical cell with a beryllium disk as current collector for the working electrode was used for *in-situ* XRD as well as for diffraction data collection over chemically lithiated and sodiated samples.[17,18] Laboratory XRD data were all collected in reflectance.

High-resolution synchrotron powder diffraction data were collected at room temperature using the 11-BM beamline at the Advanced Photon Source (APS), Argonne National Laboratory using an average wavelength of 0.413965 Å. The data were collected in the 2θ range of -6.5 to 28.0˚ with a step size of 0.001˚ and 0.1 s spent on each step. Neutron diffraction and total scattering data were collected at room temperature on polycrystalline powders loaded in a vanadium can using the time-of-flight POWGEN instrument (BL-11A) and NOMAD instrument (BL-1B), respectively, at the Spallation Neutron Source, Oak Ridge National Laboratory. POWGEN data were collected with 16 h spent on bank 3 and 4 h on bank 4. Bank 3 uses frame #1.5 at 60 Hz with a Q range of 1.1688 $Å^{-1}$ to 15.1700 $Å^{-1}$ and bank 4 uses frame #1.75 at 60 Hz with a Q range of 0.6820 $Å^{-1}$ to 5.6923 $Å^{-1}$. Data from all detectors with angles from 20 to 150˚ were combined into one histogram for each bank. NOMAD data were collected in the scattering angle range of 3 to 175˚ with 40 min spent on each sample. Data from all detectors were reduced into one PDF pattern after the

background contribution was subtracted. The resulting data were analyzed using the General Structure Analysis System (GSAS)[19] and PDFgui.[20]

Electrochemical measurements

Electrochemical measurements were carried out using Swagelok-type cells.[18] The positive electrodes were prepared by grinding $Fe_2(MoO_4)_3$ and carbon Super P (CSP) for 30 min in an Ar-filled glove box. A slurry was prepared by adding the resulting mixture into polyvinylidenefluoride (PVDF) dissolved in *N*-methyl-2-pyrrolidone (NMP). The slurry, comprised of 76.4 wt% $Fe_2(MoO_4)_3$, 8.5 wt% CSP, and 15.1 wt% PVDF, was cast onto an aluminum foil and dried in a vacuum oven at 110 ˚C overnight. Electrodes were peeled off the Al foil and punched into 1.0 cm diameter circles.

Li or Na metal disks were used as the negative electrodes. Whatman GF/D borosilicate glass fiber sheets were used as the separator and soaked in electrolyte solution of either 1 M $LiPF_6$ in ethylene carbonate (EC), propylene carbonate (PC), and dimethylcarbonate (DMC) (45:45:10 by weight) or 1 M $NaClO_4$ in EC and DMC (1:1 by weight).

Symmetry-mode analysis

Symmetry-mode analysis was carried out using the *AMPLIMODES* program of the Bilbao Crystallographic Server.[21] The inputs of the program include structural parameters of a high-symmetry and a low-symmetry structure. Results from Rietveld refinements against synchrotron X-ray and neutron diffraction data on pristine and Li^+-inserted $Fe_2(MoO_4)_3$ were used as low-symmetry and high-symmetry phases, respectively.

X-ray photoelectron spectroscopy (XPS)

The high-resolution XPS spectrum was acquired using a Kratos Axis Ultra X-ray photoelectron spectrometer with the analyzer lens in hybrid mode. A monochromatic

aluminum anode with an operating current of 6 mA and voltage of 10 kV was used with a step size of 0.1 eV, a pass energy of 20 eV, and a pressure range between 1×10^{-8} torr to 3×10^{-8} torr. The binding energy was referenced to the C1*s* core level at 284 eV.

Raman spectroscopy

Raman spectra were recorded in the 200–1200 cm^{-1} range using a Horiba Xplora Raman microscope (Horiba Scientific). Laser irradiation of 532 nm wavelength was employed as the excitation source and the power at the sample level was 50 mW. All spectra were recorded under ambient conditions, a quartz cell was used for the measurement of lithiated and sodiated samples. Intercalated samples were loaded into the quartz cell in an Ar-filled glove box.

Computational

Density functional theory (DFT) calculations were performed using the plane-wave code VASP.[22,23] Interactions between core and valence electrons were described with the PAW method, with cores of [Kr] for Mo, [Ar] for Fe, [He] for O, and [Ne] for Na.[24] All calculations used the PBEsol exchange–correlation functional.[25] To describe the strongly correlated Fe 3*d* electrons, we applied a Hubbard-type "+*U*" correction of U_d = 4.3 eV, using the rotationally invariant approach of Dudarev *et al.*[26] This value of U_d = 4.3 eV was chosen for consistency with previous calculations of orthorhombic Li^+- and Na^+-inserted $Fe_2(MoO_4)_3$ by Yue *et al.*[15] who, in turn, selected this value from earlier calculations on Li_xFePO_4.[27] A planewave cutoff of 550 eV was used, and all calculations were spin-polarized. High spin Fe was assumed, extrapolating from calculations of the parent monoclinic $Fe_2(MoO_4)_3$ phase that predicted a high-spin anti-ferromagnetic solution. All structures were geometry-optimized with no assumed symmetry by performing a series of constant volume structural relaxations, and fitting the resultant data to the Murnaghan equation of

state. Individual geometry optimizations were deemed converged when all atomic forces fell below 0.01 eV $Å^{-1}$. Orthorhombic $Li_2Fe_2(MoO_4)_3$ was modeled using a single unit cell (76 atoms), with 2 × 2 × 2 Monkhorst-Pack *k*-point sampling, using our Rietveld-refined structure as a starting configuration. Because we were unable to directly refine the monoclinic $Na_2Fe_2(MoO_4)_3$ structure, an approximate structure used to initialize the DFT geometry optimization was constructed by projecting the optimized $Li_2Fe_2(MoO_4)_3$ structure onto a (1 × 2 × 1)-expanded monoclinic cell (152 atoms). The structural relaxation of the Na^+-intercalated phase used a 2 × 1 × 2 Monkhorst-Pack *k*-point grid.

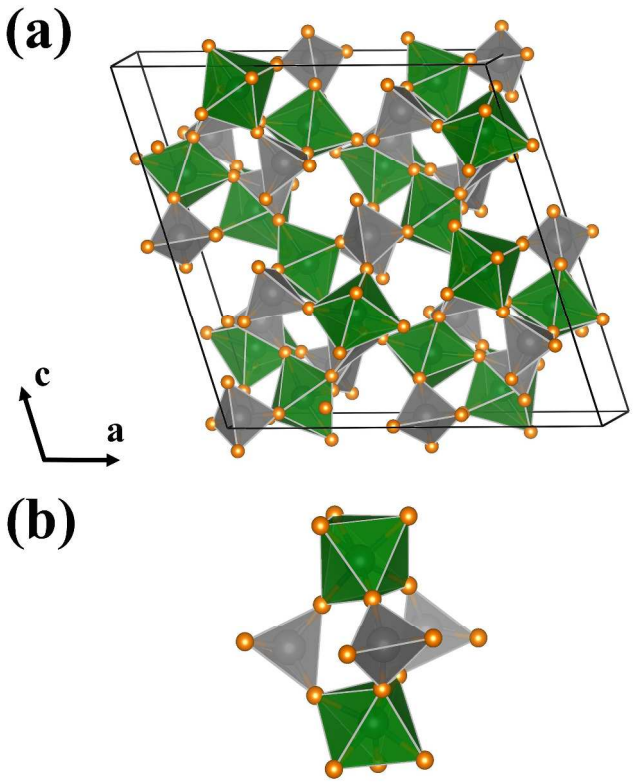

Figure 1. Illustration of (a) the unit cell of pristine, monoclinic $Fe_2(MoO_4)_3$ and (b) a "lantern unit" that consists of three MoO_4 tetrahedra connecting two FeO_6 octahedra.

Results

Pristine $Fe_2(MoO_4)_3$ was prepared by a precipitation method following the approach of Peng *et al.*[16] After annealing at 400 ˚C for 6 h, the phase-pure powder possessed a nanorod-like morphology (Supporting Information, Figure S1). Figure 2 shows the results of the Rietveld refinement of the monoclinic $P2_1/c$ structure against the synchrotron X-ray (Figure 2a) and neutron diffraction (Figure 2b) patterns of the as-prepared $Fe_2(MoO_4)_3$ electrode material. The diffraction patterns were refined simultaneously with structural parameters starting from the model of Chen *et al.*[28] Detailed structural parameters including atomic positions, cell parameters, and anisotropic displacement parameters are given in the Supporting Information (Table S1). Both diffraction patterns could be fully indexed to lattice planes from the expected monoclinic phase without any evidence of impurity peaks, confirming that the parent $Fe_2(MoO_4)_3$ utilized throughout this study was phase pure. Raman spectroscopy showed that the as-prepared $Fe_2(MoO_4)_3$ possessed bands characteristic of the monoclinic structure at 988, 967, 930 cm^{-1} (symmetric stretching modes of terminal Mo=O bonds in three distinct MoO_4 tetrahedra); 817, 776 cm^{-1} (asymmetric stretching modes of MoO_4 units); and 356 cm^{-1} (MoO_4 bending mode) (Supporting Information, Figure S2).[29] X-ray photoelectron spectra (XPS) of the Fe2*p* and Mo3*d* regions suggest there is only one chemical environment for both Fe and Mo in the pristine, as-prepared $Fe_2(MoO_4)_3$ by the presence of characteristic Fe^{3+} $2p_{3/2}$ and Mo^{6+} $3d_{5/2}$ peaks with binding energies of 711.3 eV and 232.5 eV, respectively (Supporting Information, Figure S3).[30,31]

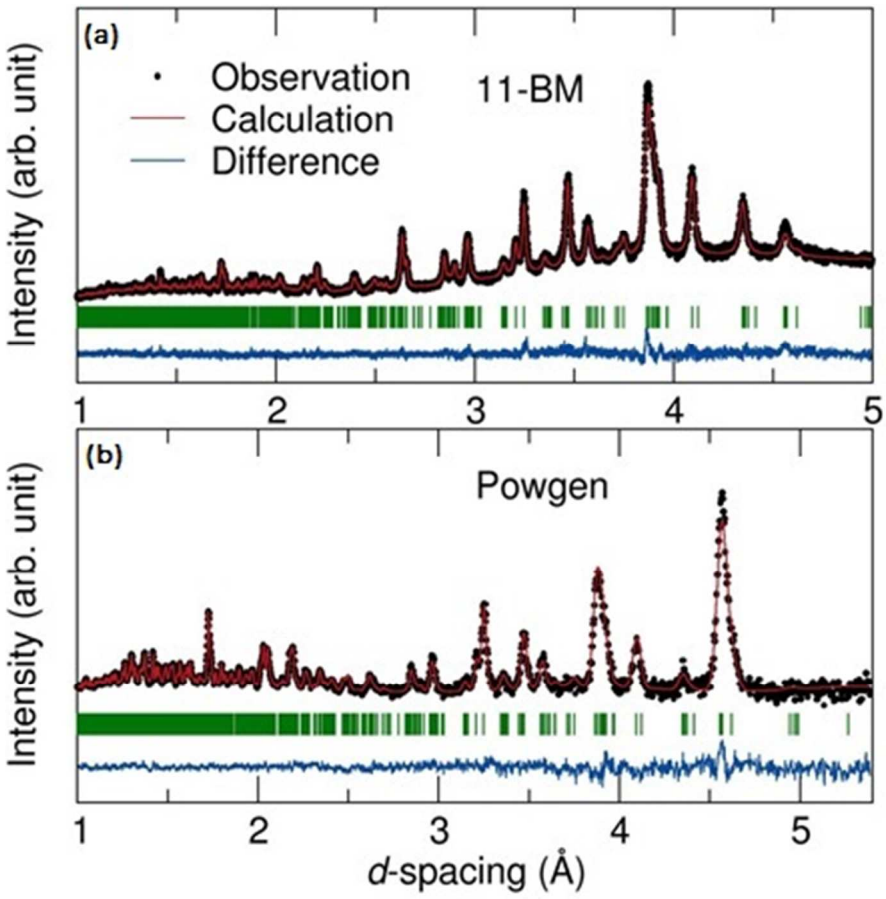

Figure 2. Rietveld refinements of pristine, monoclinic $Fe_2(MoO_4)_3$ against (a) synchrotron XRD pattern obtained at the 11-BM beamline at Argonne National Laboratory and (b) neutron diffraction pattern obtained at the POWGEN beamline at Oak Ridge National Laboratory. The weighted profile *R*-factor (R_{wp}) was determined to be 6.01% for all banks being refined simultaneously and weighed equally. Absorption correction was carried out using absorption function 0 in GSAS. Only the diffraction pattern from bank 3 at POWGEN is given here.

Li^+ insertion

The first ten galvanostatic electrochemical cycles of $Fe_2(MoO_4)_3$ against Li/Li^+ at a current rate of C/10 are given in Figure 3a. The initial specific capacity of 92 $mA{\cdot}h{\cdot}g^{-1}$ agrees well with the theoretical capacity of intercalation of two Li^+ ions per formula unit (90 $mA{\cdot}h{\cdot}g^{-1}$), with the slight excess capacity likely associated with the formation of a passivating solid electrolyte interface layer.[32] Without rigorous optimization of the cell assembly, the batteries showed a high capacity retention of around 90% of the initial capacity after 25 cycles (Supporting Information, Figure S4). The derivative of the

galvanostatic cycling (inset of Figure 3a) shows two peaks centered at 3.0 V and 3.05 V during reduction and oxidation, respectively. Such a small polarization is reflective of the highly reversible intercalation of Li^+ into the framework of $Fe_2(MoO_4)_3$. The voltage-composition curve exhibits a single plateau over a wide range of lithium content during Li^+ (de)insertion, which indicates the intercalation process predominantly occurs through a two-phase process where a lithium-rich phase is created directly rather than a solid-solution process, since there is a continuous change in the lithium content throughout each particle.[11]

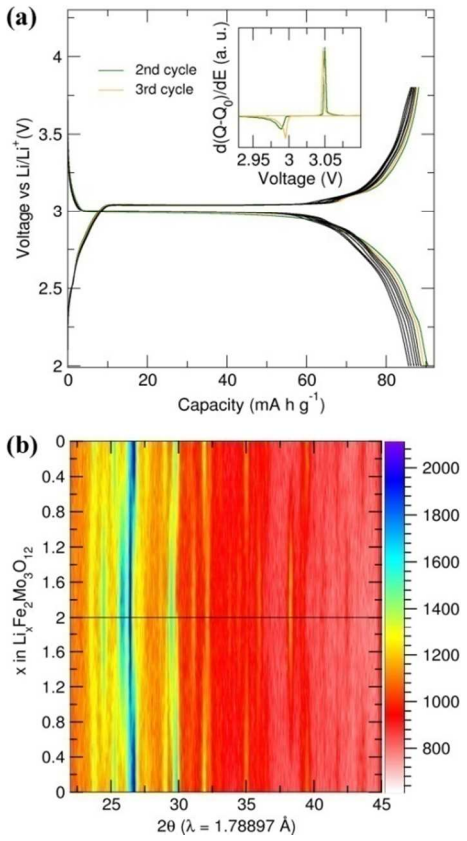

Figure 3. (a) Galvanostatic electrochemical cycling of $Fe_2(MoO_4)_3$ against Li^+ insertion and its derivative (shown as inset). (b) 2D pattern based on the *in-situ* XRD of Li^+ insertion into $Fe_2(MoO_4)_3$.

The coexistence of two phases was further demonstrated using *in-situ* X-ray diffraction, taken continuously during electrochemical cycling, and is shown as a heat map in Figure 3b with the *y*-axis corresponding to the equivalents of inserted Li^+. During the discharging process, new reflections at 24.5°, along with several others at 36° and 38.5°, clearly appear (Supporting Information, Figures S5 and S6). The intensity of other reflections (*e.g.*, at 23.5°, 36.8°, and 39.8°) gradually decreases until finally disappearing as the Li^+ content increases. As shown in the Supporting Information in Figure S6, all reflections of the fully electrochemically lithiated phase, except those contributed by the beryllium cell used for the *in-situ* measurements, can be indexed to the orthorhombic $Li_2Fe_2(MoO_4)_3$ phase originally reported by Torardi *et al*.[33]

During the charging process, changes in the intensities of reflections were observed exactly in the opposite way, indicating excellent structural reversibility upon Li^+ (de)insertion. Positions of the reflections do not vary with Li^+ insertion in the pristine $Fe_2(MoO_4)_3$, which excludes the possibility of a solid solution process. These changes in the intensities of reflections are illustrative of the evolution of the initial monoclinic $Fe_2(MoO_4)_3$ structure into orthorhombic $Li_2Fe_2(MoO_4)_3$ with the increasing Li^+ content, and the coexistence of pristine and lithiated structures in various ratios depending on the Li^+ concentration. Thus, a two-phase Li^+ (de)insertion process in the anti-NASICON $Fe_2(MoO_4)_3$ was confirmed for the first time through *in-situ* XRD.

The crystal structure of orthorhombic $Li_2Fe_2(MoO_4)_3$ (Supporting Information, Figure S7) shows an identical structural topology to the parent monoclinic phase with regards to polyhedral connectivity, so the transformation is purely displacive in nature. While the *in-situ* XRD experiments provide some insight into the mechanism for these displacements, the patterns do not have sufficient resolution or intensity to precisely refine changes in the atomic positions. Therefore, $Fe_2(MoO_4)_3$ was chemically lithiated as discussed in the experimental section. The results of the Rietveld refinement of the inserted structure against synchrotron X-ray and neutron diffraction data is shown in the Supporting Information in Figure S8 with detailed structural parameters listed in Table S2. To describe the transition between the monoclinic and orthorhombic structures in terms of the reversible symmetry-allowed distortions, the *AMPLIMODES* program at the Bilbao

Crystallographic Server[21] was used to identify the transformation matrix (given in Supporting Information, Table S3) for the transition from the low-symmetry ($P2_1/c$) pristine structure to the higher-symmetry (*Pbcn*) lithiated structure. The vectors corresponding to the direction of the displacements for each element were calculated and are illustrated in Figure 4. A complete list of the vectors is given in the Supporting Information, Tables S5 and S6.

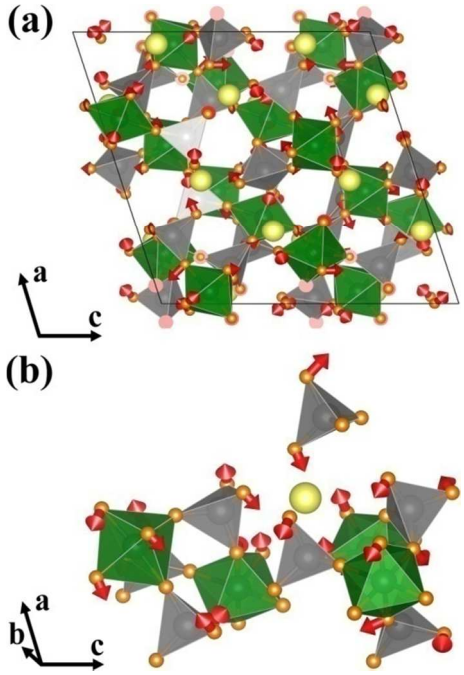

Figure 4. Amplimodes analysis between pristine $Fe_2(MoO_4)_3$ and lithiated $Li_2Fe_2(MoO_4)_3$, with positions of Fe, Mo, and O in pristine $Fe_2(MoO_4)_3$ and position of Li in $Li_2Fe_2(MoO_4)_3$ converted into the same reference structure setting. The transformation vectors are plotted on each atom in (a) and filtered by amplitude of 0.4 Å in (b) for clarity. FeO_6 octahedra are shown in green, and MoO_4 tetrahedra are shown in gray. Li^+ ions are left out for amplimodes analysis, but are drawn in the reference structure for clarity.

The most prominent displacement seen from these vectors are those associated with oxygen atoms. The vectors on Fe and Mo atoms are extremely small, indicating that the center of mass for the rigid polyhedral subunits remains fixed as they rotate to enlarge the unit cell volume. It is interesting to note, as shown in Figure 4b, that Li^+ ions are inserted between two neighboring lantern units and, as a result, there are significant displacement of the oxygen atoms toward the guest ions, presumably a consequence of local bonding or

electrostatic interactions. This suggests that the ability for the framework to distort in such a way that Li–O interactions can form and break in a reversible fashion is an important consideration in the design of efficient intercalation hosts.

Na^+ insertion

Figure 5a shows the galvanostatic cycling of $Fe_2(MoO_4)_3$ against Na/Na^+. An initial capacity of 79 $mA{\cdot}h{\cdot}g^{-1}$ was found, which corresponds to the insertion of 1.7 Na^+ per $Fe_2(MoO_4)_3$, which is comparably smaller than that observed with Li^+ insertion (Supporting Information, Figure S4). The capacity was found to drop to 87% of the initial capacity after 20 cycles, showing a similar capacity retention to that of the $Li/Fe_2(MoO_4)_3$ cell. The most pronounced difference from Li^+ insertion is that there are two distinct slope regions during the Na^+-intercalation process instead of a single plateau. This is signified by two peaks (centered at *ca*. 2.7 V and 2.58 V) in the derivative curve given as the inset of Figure 5a. The reproducibility of these peaks with respect to cell potential during subsequent cycles demonstrates that the Na^+ de(insertion) process is also highly reversible, and the electrochemical profile is intrinsic to the Na^+-intercalation process.

The *in-situ* XRD experiments during Na^+ intercalation showed substantial differences compared to that of Li^+ insertion. During discharge, a constant shift in the Bragg reflections toward lower angles was observed with all the peaks returning to their original positions after fully charging. This shift corresponds to the expansion of the unit cell volume in order to accommodate the guest alkali cations during the insertion process, but given that no new reflections evolve during cycling, this indicates that a solid solution mechanism is at play, in contrast to the biphasic process described for lithium.

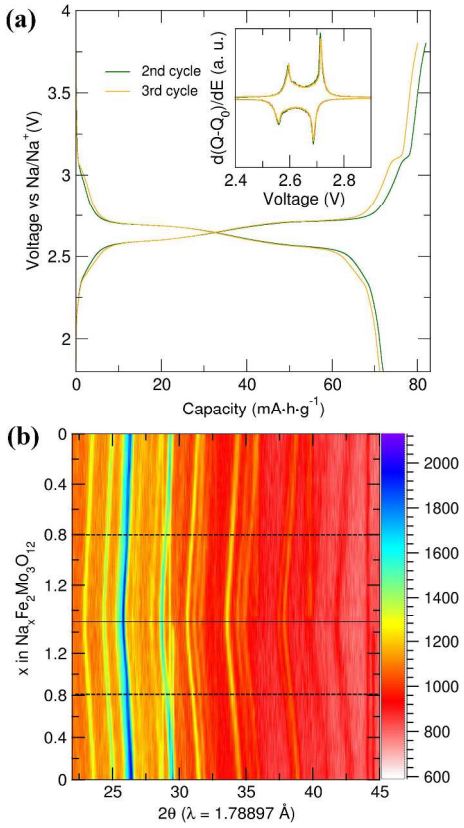

Figure 5. (a) Galvanostatic electrochemical cycling of $Fe_2(MoO_4)_3$ against Na^+ insertion and its derivative (shown as inset). There are two slope regions during both insertion and de-insertion. The turn from one region to the other corresponds to 0.8 Na^+ per formula being (de)inserted. (b) 2D pattern based on the *in-situ* XRD of Na^+ insertion into $Fe_2(MoO_4)_3$.

While the laboratory XRD patterns did not provide enough intensity to allow for a full refinement of the atomic positions, it was possible to track changes in the unit cell using Le Bail fits to the inserted patterns. Relative changes in these parameters are plotted in Figure 6 with a complete list of the refined lattice parameters given in the Supporting Information, Table S7. A volume change of 6% was found for insertion of 1.5 Na^+ ions per formula unit, with the dominant change in the unit cell corresponding to a roughly 4% elongation of the *b*-axis. While the magnitude of the change along the *a*- and *c*-axes is less pronounced, the trend seems to suggest the underlying insertion mechanism. The *c*-axis does not significantly change during the initial stages of Na^+ insertion, while the *a*-axis exhibits a continuous extension. After the insertion of 0.8 Na^+ per formula unit, the trends are reversed (*i.e.*, the change in *a*-axis flattens out while the *c*-axis shows a continuous

increase). It is also important to recognize that the unit cell parameters of the Na^+ intercalated monoclinic phase and the orthorhombic structure identified for $Li_2Fe_2(MoO_4)_3$ suggests that the parent framework of $Fe_2(MoO_4)_3$ actually rotates in the same way regardless of Li^+ or Na^+ insertion. The primary difference between the two space group choices depends heavily on the position where the guest ions end up sitting. Within this context, the pronounced elongation of the *b*-axis is probably the result of the larger Na^+ ions relative to that of Li^+ and that the size of the intercalant plays a crucial role in determining how the structure can distort.

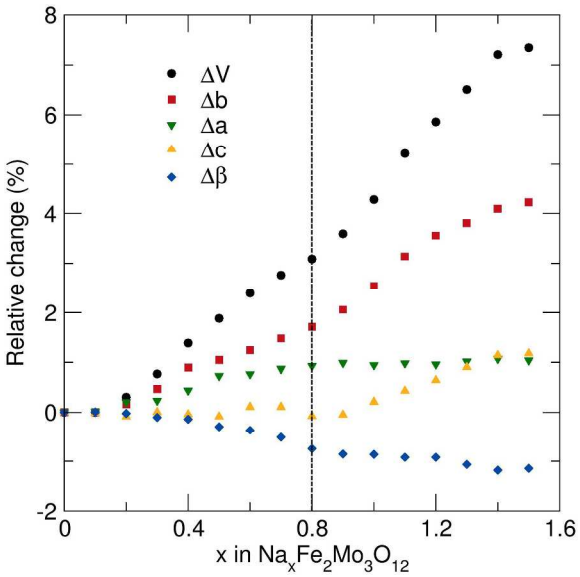

Figure 6. Lattice evolution along Na^+ insertion into $Fe_2(MoO_4)_3$ from Le Bail fitting of *in-situ* X-ray diffraction patterns.

Given the complexity of the monoclinic structure, which contained 34 unique atomic positions and over 150 refinable parameters, it proved impossible to directly refine the structure of Na^+-inserted $Fe_2(MoO_4)_3$ by starting from the model of the pristine structure. Therefore, we turned to density functional theory calculations to obtain a predicted structure for monoclinic $Na_2Fe_2(MoO_4)_3$, which was used for further Rietveld refinement. We first calculated an optimized structure for orthorhombic $Li_2Fe_2(MoO_4)_3$, starting from the experimentally determined geometry. This gave excellent agreement with the Rietveld refined geometry (*e.g.*, lattice parameters agree to within 0.5%), which demonstrates that

our PBEsol+U calculations are able to well describe the structure for this high-symmetry lithium-ordered phase. The atomic positions from the DFT-optimized orthorhombic $Li_2Fe_2(MoO_4)_3$ were then projected onto a monoclinic cell as a starting structure for the $Na_2Fe_2(MoO_4)_3$ structure optimization. The calculated Li^+-inserted and Na^+-inserted structures from the simulations are included in the Supporting Information, Tables S8 and S9. Despite the extremely good agreement between the DFT cell for the lithiated compound and its experimentally determined structure, there is a striking difference between the increase of the unit cell volume for Na^+-insertion predicted by DFT (16.0%) and that found experimentally (6.0%). Notwithstanding this discrepancy, the DFT-optimized $Na_2Fe_2(MoO_4)_3$ structure generates a close match for the peak position and intensities in the neutron diffraction data (Supporting Information, Figure S9). Using the DFT-optimized structure for subsequent Rietveld refinement, however, produces unphysically large atomic displacement parameters for the sodium atoms. These large displacement parameters indicate that the intensity contributed to the pattern by Na^+ is negligible, and suggests a more complex distribution of sodium ions in the experimental sample. Refining the optimized structure again after removing sodium atoms produces a fit nearly identical to the refinement with the sodium included (Supporting Information, Figure S10). The resulting framework is illustrated in the Supporting Information, Figure S11 with the full structural description listed in Table S10.

There are two possible explanations for the lack of scattered intensity associated with the sodium atom positions. Either the Na^+ ions are disordered through the lattice, or they adopt some kind of long wavelength superstructure that is not immediately obvious in the powder diffraction experiment. Considered alongside the erroneous predicted volume increase for the DFT-optimized structure, these results suggest that the calculated volume expansion is a consequence of an (artificial) ordering of Na^+ within the polyanion framework. The use of a (1 × 2 ×1) periodic cell for the DFT calculations imposes an

artificial symmetry on the Na^+ ions, and this may block a fully disordered sodium configuration, instead predicting an ordered Na^+-inserted structure. The larger size of Na^+ versus Li^+, however, means this Na^+ ordering can only be accommodated within the polyanion framework through a significant volume expansion. This conceptual model predicts that the smaller volume expansion and apparent Na^+ disorder observed in the experimental refined structure are coupled. We propose that in the experimental system the lattice strain produced by intercalating large Na^+ ions could be accommodated by a disordering of these ions, rather than the otherwise necessary volume expansion predicted in the higher symmetry DFT calculations. In contrast, smaller Li^+ ions are able to occupy an ordered arrangement of sites upon intercalation, without imposing a large volume change, leading to highly consistent DFT-predicted and experimental structures. The inability of our DFT calculations to predict structures in close agreement with those obtained from experiment for Na^+-inserted $Fe_2(MoO4)_3$ indicates the limitations of standard periodic zero-temperature calculations for modeling disordered intercalation phases, and suggests alternative approaches that consider thermally disordered systems, such as large-scale molecular dynamics, may be necessary to obtain a detailed atomic-scale description of these disordered ions.

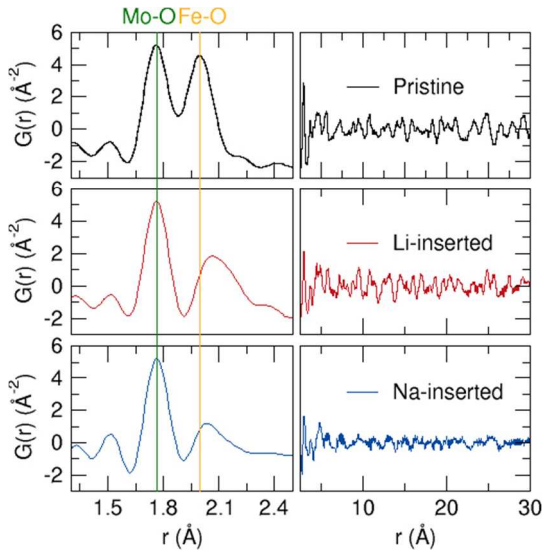

Figure 7. Experimental total scattering data for pristine, Li^+-inserted, and Na^+-inserted $Fe_2(MoO_4)_3$.

To further characterize the nature of the insertion process on the local structure of $Fe_2(MoO_4)_3$, total neutron scattering data was collected on the pristine and chemically inserted samples (Figure 7). The peak observed at 1.76 Å, which corresponds to the Mo–O interatomic distance within the MoO_4 tetrahedra, does not change at all after Li^+/Na^+ insertion. This is consistent with the more covalent and therefore more rigid nature of the MoO_4 tetrahedra. In contrast, there is a very significant elongation of the Fe–O bonds that should be expected as the oxidation state of Fe changes from 3+ to 2+ upon insertion of the alkali ions. It is also interesting to point out that that the long range correlations, especially those at long *r* values > 3 Å, are significantly more dampened in the Na^+ inserted phase than that of the pristine or Li^+-inserted phases. This reflects the local disorder that results as a consequence of the interactions with the complex distribution of Na^+ through the lattice.

Finally, Raman spectra of Li^+- and Na^+-inserted $Fe_2(MoO_4)_3$ were collected to determine if signatures of the disorder could be identified (Supporting Information, Figure S2). Both the lithiated and sodiated samples show Raman bands belonging to the MoO_4 units that appear to be either weak or unresolved. The strongest asymmetric stretching band of the MoO_4 units in the Raman spectrum of the pristine material appears to be very broad and weak in the spectra of lithiated and sodiated samples. However, the weaker bending and symmetric stretching modes remained unresolved. In addition, no shift in the positions of Raman bands was observed. This broadening and loss of intensity may be attributed to the redistribution of electron density in the Mo–O bonds through the intercalation of alkali guest ions into the pristine material, which may also be affected by the reduction of Fe^{3+} ions to Fe^{2+}.[34,35] Therefore, the effective force constants and polarizability derivatives may be varied as the electron density is redistributed, resulting in the observed broadening and intensity loss in the Raman bands. The major difference was observed in the asymmetric

stretching band of MoO_4 tetrahedra. The intensity of the strongest asymmetric stretching mode at 776 cm^{-1} was found to be lower than of the second asymmetric stretching mode at 817 cm^{-1} in the intercalated samples. This suggests that strong interactions between alkali ions and the polyhedral oxygen ions results in changed intensities for stretching motions in the MoO_4 units, while the framework remains largely the same.

With a description of the Li^+- and Na^+-inserted phases of $Fe_2(MoO_4)_3$, a comparison between the changes to the structural frameworks should provide insight into the mechanism for intercalation. A representative portion of the refined framework with lithium determined by $Li_2Fe_2(MoO_4)_3$ refinement is illustrated in the Supporting Information, Figure S12. To understand how the polyhedral rotations are affected by the alkali ions, a set of dihedral angles are calculated from the structural models. The center atoms of two connected polyhedra form two planes with one oxygen atom from each of the polyhedra in these dihedral angles, which thus measures the relative rotational displacement between the two polyhedra. For example, the tweaking between the FeO_6 octahedra and MoO_4 tetrahedra can be measured by the dihedral angles of such as O2-Mo2-Fe1-O5. A complete list of the dihedral angles between these two polyhedra is given in the Supporting Information, Table S11. It can be seen there is a difference in every dihedral angle between the Na^+-inserted and Li^+-inserted $Fe_2(MoO_4)_3$, and a difference smaller than 2° can be considered as systematic residuals. There are more significant differences, such as the 3° difference in the O2-Mo2-Fe1-O5 and O2-Mo2-Fe1-O6 angles. From our symmetry mode analysis, the transformation from the pristine to the inserted phase is accompanied by oxygen atoms moving towards the inserted ion (Li^+), possibly driven by a strong electrostatic Li–O interaction. Thus, as O5 on the bottom left corner in Figure S12 moves towards the alkali ion, driving the FeO_6 to rotate in a way that essentially results in O5 and O6 moving away from O2 in the MoO_4 tetrahedra on the top left corner, and because the Li–O bond is shorter than the Na–O bond, the dihedral angle of O2–Mo2–Fe1–O5 is larger and

that of O2–Mo2–Fe1–O6 is smaller in Li^+-inserted $Fe_2(MoO_4)_3$ than Na^+-inserted phase. This again highlights that while a striking difference has been observed in the electrochemical cycling curves, as well as structural phase changes between the Li^+- and Na^+-intercalation in $Fe_2(MoO_4)_3$, the fundamental mechanism for Li^+- and Na^+-intercalation is effectively the same but structural differences arise because of the differences in ionic radii.

Discussion

We have investigated the insertion mechanisms of two different alkali guest ions into the $Fe_2(MoO_4)_3$ framework and found that the ability for the framework to distort *via* cooperative rotations may be important for facilitating intercalation. This has been confirmed by the symmetry-mode analysis of pristine and Li^+-inserted $Fe_2(MoO_4)_3$, and through careful analysis of the total scattering data on both Li^+- and Na^+-inserted samples. Similar observations have been found in $LiFeSO_4F$ cathode materials,[36–38] and the lack of connection between these two structure types implies that such a mechanism may have wider applications in understanding polyanionic electrode materials. It should also be noted that the distortion through rigid and strongly covalently bonded polyhedra restricts the way the host structure can distort, and thus offers better longevity than oxide materials, which usually suffer from drop in performance due to severe structural changes during cycling.[39,40]

While the mechanism of polyhedral rotational distortion we have proposed has not been widely discussed with respect to intercalation electrodes, it has been extensively explored in the superionic conductor literature.[41–43] This is typically found in studies of two competing mechanisms: (i) a “paddle wheel” mechanism, which suggests a strong correlation between the transport of cations and the rotation of polyhedral subunits, and (ii) a “percolation” mechanism, which claims independence between conduction pathway and polyhedral rotations.[41,42] For example, through powder neutron diffraction and reverse

Monte Carlo (RMC) modeling, Karlsson *et al.* revealed that both types of mechanisms are present in high-temperature forms of Li_2SO_4 and $LiNaSO_4$.[41,43]

These rotational distortions may suggest a more generalized mechanism for alkali ion intercalation in polyanionic materials, but more importantly, this work has revealed a difference in the behavior between Li^+- and Na^+-intercalation into the same host, which suggest that differences in the intrinsic nature of Li^+ and Na^+ guest ions may result in a modification of such a mechanism. We observed a two-stage, solid solution Na^+ insertion process as compared to a single, two-phase Li^+ insertion process, which is similar to what has been found in olivine-type $FePO_4$ and explained by stronger interactions of Na^+ ions as compared to Li^+ ions with the host structure by Moreau *et al.*[44] Our results also indicate that the two redox peaks in $Fe_2(MoO_4)_3$ do not appear to correspond to the complete filling of two distinct Na^+ positions, but rather that the distribution of Na^+ ions is much more nuanced. There are two possible explanations for the lack of scattered Bragg intensity. First is that the Na^+ ions are disordered through the lattice. This disorder could be the result of two discrete crystallographic positions, each having a distinct chemical potential for the alkali ion, but as the framework rotates and distorts to accommodate more ions the Na^+ ions already in the framework are pushed off their ideal position. Second is that the Na^+ ions adopt a long wavelength superstructure that cannot be seen in the powder diffraction experiment. A more careful investigation into intermediate compositions may provide more valuable information in this regard, but a comparison between the total neutron scattering data on Li^+- and Na^+-inserted $Fe_2(MoO_4)_3$ shows that peaks at high *r* values are less intense in Na^+-inserted sample than those in Li^+-inserted sample, which reinforces the notion that the rotational distortions are less coherent following Na^+ than Li^+ insertion. Both explanations could result from the larger ionic size of Na^+ than Li^+, and thus a steric hindrance for the rotational distortions to allow the Na^+ ions to find an ideal position.

Finally, we note that the highly insulating character of these materials would require that the charge transport through the lattice would have to be mediated through some kind of polaronic hopping of the electrons. It could be possible that the structural distortions reported here are related to this mechanism of charge hopping, and further work using X-ray absorption spectroscopy may be useful in elucidating this aspect of the transport properties.

Conclusions

In summary, we have presented a detailed structural characterization of the process by which Li^+ and Na^+ ions intercalate into $Fe_2(MoO_4)_3$, and how these structural transformations are related to the correlated rotations of rigid polyanionc subunits. The combination of electrochemical cycling and *in-situ* powder XRD confirmed a two-phase process for Li^+-intercalation, compared to a two-stage solid solution insertion process for Na^+-intercalation, which corresponds to Na^+ filling two different sites. Furthermore, based on our Rietveld refinements, symmetry-mode analysis and examination of neutron total scattering data, we proposed a concerted polyhedra rotational distortion mechanism for the alkali guest ion intercalation into the anti-NASICON $Fe_2(MoO_4)_3$ host framework. It is also shown that during Li^+-insertion, Li^+ ions fill defined positions that allow the transformation from the pristine monoclinic phase to the lithiated orthorhombic structure. However, Na^+ insertion occurs in a more complex manner that appears to result from the larger size of Na^+ compared to Li^+. Such a mechanism, as well as the application of symmetry-mode analysis along with structural and electrochemical characterization, may be applied to other polyanionic material systems. Insights gained through these analyses may facilitate the discovery of new intercalation materials and the improvement of existing ones.

Acknowledgements

G.B. and R.L.B. acknowledge funding through the Department of Energy Office of Basic Energy Sciences under Grant No. DE-FG02-11ER46826. S.Z. and B.C.M. gratefully acknowledge support through a CAREER award from the National Science Foundation under Grant No. DMR-1554204. B.J.M. acknowledges support from the Royal Society (UF130329). Use of the Advanced Photon Source at Argonne National Laboratory was supported by the U.S. Department of Energy, Office of Science, Office of Basic Energy Sciences, under Contract No. DE-AC02-06CH11357. Neutron diffraction studies were supported by the Office of Basic Energy Sciences, U.S. Department of Energy, at the Spallation Neutron Source, Oak Ridge National Laboratory under contract DEAC05-00OR22725 with UT Battelle. This work made use of the ARCHER UK National Supercomputing Service (http://www.archer.ac.uk), via the membership of the UK's HPC Materials Chemistry Consortium, funded by EPSRC (EP/L000202).

Supporting Information:

Additional experimental details, TEM images, x-ray photoelectron and Raman spectra of pristine and chemically inserted $Fe_2(MoO_4)_3$; capacity retention of Li and Na cells, Rietveld refinement results against laboratory x-ray data on pristine and lithiated $Fe_2(MoO_4)_3$, crystal structures of $Li_2Fe_2(MoO_4)_3$, refinement results of neutron powder diffraction patterns of chemically lithiated $Li_2Fe_2(MoO_4)_3$, detailed symmetry-mode analysis results; results from our attempts to determine the structure of Na-inserted $Fe_2(MoO_4)_3$. The Supporting Information is available free of charge on the ACS Publications website at DOI://XXX

Corresponding Authors

*E-mail: melot@usc.edu

*E-mail: brutchey@usc.edu

Author Contributions

§ These authors contributed equally to this work.

References

(1) Erickson, E. M.; Ghanty, C.; Aurbach, D. New Horizons for Conventional Lithium Ion Battery Technology. *J. Phys. Chem. Lett.* **2014**, *5*, 3313–3324.

(2) Palomares, V.; Serras, P.; Villaluenga, I.; Hueso, K. B.; Carretero-González, J.; Rojo, T. Na-ion Batteries, Recent Advances and Present Challenges to Become Low Cost Energy Storage Systems. *Energy Environ. Sci.* **2012**, *5*, 5884.

(3) Dunn, B.; Kamath, H.; Tarascon, J.-M. Electrical Energy Storage for the Grid: A Battery of Choices. *Science* **2011**, *334*, 928–935.

(4) Wang, L. P.; Yu, L.; Wang, X.; Srinivasan, M.; Xu, Z. J. Recent Developments of Electrode Materials for Sodium Ion Batteries. *J. Mater. Chem. A* **2015**, *3*, 9353–9378.

(5) Xu, B.; Qian, D.; Wang, Z.; Meng, Y. S. Recent Progress in Cathode Materials Research for Advanced Lithium Ion Batteries. *Mater. Sci. Eng. Reports* **2012**, *73*, 51–65.

(6) Whittingham, M. S. Ultimate Limits to Intercalation Reactions for Lithium Batteries. *Chem. Rev.* **2014**, *114*, 11414–11443.

(7) Masquelier, C.; Croguennec, L. Polyanionic (Phosphates, Silicates, Sulfates) Frameworks as Electrode Materials for Rechargeable Li (or Na) Batteries. *Chem. Rev.* **2013**, *113*, 6552–6591.

(8) Etacheri, V.; Marom, R.; Elazari, R.; Salitra, G.; Aurbach, D. Challenges in the Development of Advanced Li-ion Batteries: A Review. *Energy Environ. Sci.* **2011**, *4*, 3243–3262.

(9) Padhi, A. K.; Manivannan, V.; Goodenough, J. B. Tuning the Position of the Redox Couples in Materials with NASICON Structure by Anionic Substitution. *J. Electrochem. Soc.* **1998**, *145*, 1518–1520.

(10) Shirakawa, J.; Nakayama, M.; Wakihara, M.; Uchimoto, Y. Changes in Electronic Structure upon Li Insertion Reaction of Monoclinic $Li_3Fe_2(PO_4)_3$. *J. Phys. Chem. B* **2006**, *110*, 17743–17750.

(11) Manthiram, A.; Goodenough, J. B. Lithium Insertion into $Fe_2(MO_4)_3$ Frameworks: Comparison of M= W with M= Mo. *J. Solid State Chem.* **1987**, *71*, 349–360.

(12) Nadiri, A.; Delmas, C.; Salmon, R.; Hagenmuller, P. Chemical and Electrochemical Alkali Metal Intercalation in the 3D-framework of $Fe_2(MoO_4)_3$. *Rev. Chim. Minérale 21*, **1984**, 537–544.

(13) Bruce, P. G.; Miln, G. Sodium Intercalation into the Defect Garnets $Fe_2(MoO_4)_3$ and $Fe_2(WO_4)_3$. *J. Solid State Chem.* **1990**, *89*, 162–166.

(14) Sun, Q.; Ren, Q.-Q.; Fu, Z.-W. NASICON-type $Fe_2(MoO_4)_3$ Thin Film as Cathode for Rechargeable Sodium Ion Battery. *Electrochem. Commun.* **2012**, *23*, 145–148.

(15) Yue, J.-L.; Zhou, Y.-N.; Shi, S.-Q.; Shadike, Z.; Huang, X.-Q.; Luo, J.; Yang, Z.-Z.; Li, H.; Gu, L.; Yang, X.-Q.; Fu, Z.-W. Discrete Li-occupation versus Pseudo-continuous Na-occupation and their Relationship with Structural Change Behaviors in $Fe_2(MoO_4)_3$. *Sci. Rep.* **2015**, *5*, 8810.

(16) Peng, C.; Gao, L.; Yang, S.; Sun, J. A General Precipitation Strategy for Large-Scale Synthesis of Molybdate Nanostructures. *Chem. Commun.* **2008**, 43, 5601–5603.

(17) Morcrette, M.; Chabre, Y.; Vaughan, G.; Amatucci, G.; Leriche, J.-B.; Patoux, S.; Masquelier, C.; Tarascon, J. M. In situ X-ray Diffraction Techniques as a Powerful Tool to Study Battery Electrode Materials. *Electrochim. Acta* **2002**, *47*, 3137–3149.

(18) Cañas, N. A.; Hirose, K.; Pascucci, B.; Wagner, N.; Friedrich, K. A.; Hiesgen, R. Investigations of Lithium–Sulfur Batteries using Electrochemical Impedance Spectroscopy. *Electrochim. Acta* **2013**, *97*, 42–51.

(19) Larson, A. C.; Dreele, R. B. V. General Structure Analysis System (GSAS); Los Alamos National Laboratory Report LAUR 86-748. *Los Alamos National Laboratory: Los Alamos, NM*, **2004**, 86 - 748.

(20) Farrow, C. L.; Juhas, P.; Liu, J. W.; Bryndin, D.; Božin, E. S.; Bloch, J.; Proffen, T.; Billinge, S. J. L. PDFfit2 and PDFgui: Computer Programs for Studying Nanostructure in Crystals. *J. Phys. Condens. Matter* **2007**, *19*, 335219.

(21) Orobengoa, D.; Capillas, C.; Aroyo, M. I.; Perez-Mato, J. M. AMPLIMODES: Symmetry-mode Analysis on the Bilbao Crystallographic Server. *J. Appl. Crystallogr.* **2009**, *42*, 820–833.

(22) Kresse, G.; Hafner, J. Norm-conserving and Ultrasoft Pseudopotentials for First-row and Transition Elements. *J. Phys. Condens. Matter* **1994**, *6*, 8245.

(23) Kresse, G.; Furthmüller, J. Efficiency of ab-initio Total Energy cCalculations for Metals and Semiconductors using a Plane-wave Basis Set. *Comput. Mater. Sci.* **1996**, *6*, 15–50.

(24) Kresse, G.; Joubert, D. From Ultrasoft Pseudopotentials to the Projector Augmented-Wave Method. *Phys. Rev. B* **1999**, *59*, 1758.

(25) Perdew, J. P.; Ruzsinszky, A.; Csonka, G. I.; Vydrov, O. A.; Scuseria, G. E.; Constantin, L. A.; Zhou, X.; Burke, K. Restoring the Density-Gradient Expansion for Exchange in Solids and Surfaces. *Phys. Rev. Lett.* **2008**, *100*, 136406.

(26) Dudarev, S. L.; Botton, G. A.; Savrasov, S. Y.; Humphreys, C. J.; Sutton, A. P. Electron-energy-loss Spectra and the Structural Stability of Nickel Oxide: An LSDA+ U Study. *Phys. Rev. B* **1998**, *57*, 1505.

(27) Zhou, F.; Marianetti, C. A.; Cococcioni, M.; Morgan, D.; Ceder, G. Phase Separation in Li xFePO$_4$ Induced by Correlation Effects. *Phys. Rev. B* **2004**, *69*, 201101.

(28) Chen, H. The Crystal Structure and Twinning Behavior of Ferric Molybdate, $Fe_2(MoO_4)_3$. *Mater. Res. Bull.* **1979**, *14*, 1583–1590.

(29) Tian, H.; Wachs, I. E.; Briand, L. E. Comparison of UV and Visible Raman Spectroscopy of Bulk Metal Molybdate and Metal Canadate Catalysts. *J. Phys. Chem. B* **2005**, *109*, 23491–23499.

(30) McIntyre, N. S.; Zetaruk, D. G. X-ray Photoelectron Spectroscopic Studies of Iron Oxides. *Anal. Chem.* **1977**, *49*, 1521–1529.

(31) Cimino, A.; De Angelis, B. A. The application of X-ray Photoelectron Spectroscopy to the Study of Molybdenum Oxides and Supported Molybdenum Oxide Catalysts. *J. Catal.* **1975**, *36*, 11–22.

(32) Lu, P.; Li, C.; Schneider, E. W.; Harris, S. J. Chemistry, Impedance, and Morphology Evolution in Solid Electrolyte Interphase Films During Formation in Lithium Ion Batteries. *J. Phys. Chem. C* **2014**, *118*, 896–903.

(33) Torardi, C. C.; Prince, E. Structure of the Lithium Insertion Compound $Li_2Fe_2(MoO_4)_3$ from Neutron Powder Diffraction Data. *Mater. Res. Bull.* **1986**, *21*, 719–726.

(34) Burba, C. M.; Frech, R. Raman and FTIR Spectroscopic Study of LixFePO$_4$ ($0 \leqslant x \leqslant 1$). *J. Electrochem. Soc.* **2004**, *151*, A1032–A1038.

(35) Melot, B. C.; Scanlon, D. O.; Reynaud, M.; Rousse, G.; Chotard, J.-N.; Henry, M.; Tarascon, J.-M. Chemical and Structural Indicators for Large Redox Potentials in Fe-based Positive Electrode Materials. *ACS Appl. Mater. Interfaces* **2014**, *6*, 10832–10839.

(36) Ellis, B. L.; Ramesh, T. N.; Davis, L. J. M.; Goward, G. R.; Nazar, L. F. Structure and Electrochemistry of Two-electron Redox Couples in Lithium Metal Fluorophosphates based on the Tavorite Structure. *Chem. Mater.* **2011**, *23*, 5138–5148.

(37) Tripathi, R.; Gardiner, G. R.; Islam, M. S.; Nazar, L. F. Alkali-ion Conduction Paths in $LiFeSO_4F$ and $NaFeSO_4F$ Tavorite-Type Cathode Materials. *Chem. Mater.* **2011**, *23*, 2278–2284.

(38) Ati, M.; Sathiya, M.; Boulineau, S.; Reynaud, M.; Abakumov, A.; Rousse, G.; Melot, B.; Van Tendeloo, G.; Tarascon, J.-M. Understanding and Promoting the Rapid Preparation of the triplite-phase of $LiFeSO_4F$ for Use as a Large-Potential Fe Cathode. *J. Am. Chem. Soc.* **2012**, *134*, 18380–18387.

(39) Melot, B. C.; Tarascon, J.-M. Design and Preparation of Materials for Advanced Electrochemical Storage. *Acc. Chem. Res.* **2013**, *46*, 1226–1238.

(40) Chung, S.-Y.; Bloking, J. T.; Chiang, Y.-M. Electronically Conductive Phospho-Olivines as Lithium Storage Electrodes. *Nat. Mater.* **2002**, *1*, 123–128.

(41) Karlsson, L. Mechanisms of Ionic Conduction in Li_2SO_4 and $LiNaSO_4$: Paddle wheel or Percolation? *Solid State Ionics* **1995**, *76*, 301–308.

(42) Keen, D. A. Disordering Phenomena in Superionic Conductors. *J. Phys. Condens. Matter* **2002**, *14*, R819–R857.

(43) Keen, D. A; Tucker, M. G.; Dove, M. T. Reverse Monte Carlo Modelling of Crystalline Disorder. *J. Phys. Condens. Matter* **2005**, *17*, S15–S22.

(44) Moreau, P.; Guyomard, D.; Gaubicher, J.; Boucher, F. Structure and Stability of Sodium Intercalated Phases in Olivine $FePO_4$. *Chem. Mater.* **2010**, *22*, 4126–4128.

Graphical TOC Entry